

Origin and Enhancement of Large Spin Hall Angle in Weyl Semimetals LaAlX ($X=\text{Si, Ge}$)

Truman Ng Yu,¹ Yongzheng Luo,^{2,†} Jiaren Yuan,^{3,‡}

Yihong Wu,⁴ Hyunsoo Yang,⁴ and Lei Shen(沈雷)^{1,2,*}

¹*Engineering Science Programme, National University of Singapore, Singapore 117575*

²*Department of Mechanical Engineering,*

National University of Singapore, Singapore 117575

³*Faculty of Science and School of Material Science and Engineering,*

Jiangsu University, Zhenjiang, China 212013

⁴*Department of Electrical and Computer Engineering,*

National University of Singapore, Singapore 117576

(Dated: March 31, 2021)

Abstract

We study the origin of the strong spin Hall effect (SHE) in a recently discovered family of Weyl semimetals, LaAlX ($X=\text{Si, Ge}$) via a first-principles approach with maximally localized Wannier functions. We show that the strong intrinsic SHE in LaAlX originates from the multiple slight anticrossings of nodal lines and points near E_F due to their high mirror symmetry and large spin-orbit interaction. It is further found that both electrical and thermal means can enhance the spin Hall conductivity (σ_{SH}). However, the former also increases the electrical conductivity (σ_c), while the latter decreases it. As a result, the independent tuning of σ_{SH} and σ_c by thermal means can enhance the spin Hall angle (proportional to $\frac{\sigma_{SH}}{\sigma_c}$), a figure of merit of charge-to-spin current interconversion of spin-orbit torque devices. The underlying physics of such independent changes of the spin Hall and electrical conductivity by thermal means is revealed through the band-resolved and k -resolved spin Berry curvature. Our finding offers a new way in the search of high SHA materials for room-temperature spin-orbitronics applications.

I. INTRODUCTION

Spin-orbitronics is a new emerging direction of spintronics, which exploits the relativistic spin-orbit coupling (SOC), and opens fascinating new roads for spin devices made of non-magnetic materials and operated without magnetic fields [1–10]. The strong SOC allows the conversion of charge current into spin current or vice versa by the spin Hall effect (SHE) in bulk nonmagnetic materials [11–15]. A direct application of charge-spin conversion is the spin-orbit torque (SOT), which utilizes the SHE to provide an ultra-fast and energy-efficient means to switch magnetization of the ferromagnets (FM) in FM/heavy-transition-metal heterostructures [3, 6, 11, 14, 16, 17]. The SOT-based devices have been widely reported, such as magnetic random access memories and spin logic devices [18]. The charge-spin conversion efficiency is described by the spin Hall angle (SHA), which is written as $\theta_{SH} = \frac{\sigma_{SH}}{\sigma_c}$ where σ_{SH} and σ_c are the spin Hall conductivity and the electrical conductivity, respectively [12, 19, 20]. High SHA is accomplished by increasing σ_{SH} and reducing σ_c values concurrently. However, it has been difficult to control each value independently. For example, the metal Pt has very

[†] mpeluoy@nus.edu.sg

[‡] 1000005084@ujs.edu.cn

* shenlei@nus.edu.sg

large σ_{SH} , but it is also an excellent conductor of electricity [21]. Semimetals usually have relative low σ_c because of their unique band feature near the Fermi level, but most of them do not have a giant SHC as Pt [22]. It has been reported that the σ_{SH} of semimetals can be significantly enhanced by electrical means, such as hole doping [19, 22]. However, their electrical conductivity will be increased, too. Increasing temperature usually reduces σ_{SH} as reported by Sun et. al. [23], meanwhile, the σ_c is reduced due to the strong electron scattering and electron-phonon coupling. Therefore, finding new materials with strong intrinsic SHE and independently tunable σ_{SH} and σ_c for enhancing SHA are highly desirable for the development of the state-of-the-art spin-orbit-torque technique.

Recently, topological insulators have shown high efficiency of charge-spin-current inter-conversion because of their large SOC and unique spin-momentum locking topological surface states [17, 24, 25]. However, the insulating bulk state is unavoidable, which strongly affects the performance of topological insulators in the application of spin-orbit torque, and their reported effectiveness in the experiment as spin Hall materials is debated. For example, the reported θ_{SH} are vary widely ranging from 0.0001 to 425 even though the experimental techniques are the same. [17, 24, 25]. Weyl semimetals (WSMs), the cousin of topological insulators, are conductors and have similar spin-momentum locking in both surface and bulk states [26, 27]. WSMs feature Dirac-like cones in their bulk near the Fermi energy (E_F) through nodal lines or points (Weyl points) on or near some crystalline planes of symmetry, such as mirror planes. Some nodal lines and points are not protected by crystalline symmetry, so these are gapped out by the SOC that is intrinsic in these materials. The sign of the spin Berry curvature (SBC) is opposite on either side of the gap, which cannot be cancelled out if the Fermi level is in or very close to the gap. As we will show below, such gapped nodal lines/points generate large spin Hall conductivity as the intrinsic SHC is proportional to the integration of the SBC of the occupied bands below E_F . Recent theoretical studies on Weyl/Dirac semimetals, such as TaAs [23], IrO₂ [28], WTe₂ [22], β -W [19], W₃Ta [29], PtTe₃ [15], and ZrSiTe [30] show large spin Hall conductivities and spin Hall angles, and some have been verified in experiments [3, 13, 31].

Very recently, a family of type-II Weyl semimetals in rare earth compounds was reported in the experiment [32–37]. These lanthanide based compounds have a chemical formula such as RAIX where (R = La, Ce, Pr) and (X = Si, Ge). Unlike La-based compounds, Ce- and Pr-based compounds are ferromagnetic in nature due to the strong electron correlations

in the 4f orbital, which breaks the time-reversal symmetry (\mathcal{T}) with the anomalous Hall effect [33, 34, 36]. The nonmagnetic Weyl semimetals LaAlSi and LaAlGe have four mirror planes and thus possess many nodal lines together with Weyl points near the Fermi level [34, 35, 37]. Furthermore, experimental results indicate that they have moderate electrical conductivity [34, 35]. Thus, it is naturally expected the existence of a high intrinsic SHC and large SHA in this new family of Weyl semimetals.

In this article, we investigate the intrinsic spin Hall conductivity, electrical conductivity and spin Hall angle of LaAlSi and LaAlGe using the first-principles calculations, Kubo formula, Boltzmann transport equation (BTE) and electron-phonon Wannier (EPW) approach. We indeed observe a large SHC in both WSMs, which originates from multiple slightly SOC-induced nodal gaps (anticrossings) near the Fermi level. It is further found that a small shift of the chemical potential below E_F by 0.12 eV, in the form of hole doping, yields a higher SHC than that of E_F . The calculated electrical and spin-Hall conductivity cooperatively yield a spin Hall angle of 0.04 and 0.046 in LaAlSi and LaAlGe respectively, which is comparable with Pt. The rest of this paper is organized as follows. In [Sec.II](#), the theory and computational details are provided. The results and discussion in [Sec.III](#) have five subsections. We first present the geometrical and electronic structures in [Sec.III A](#) and [Sec.III B](#). In the [Sec.III C](#) and [Sec.III D](#), we report the spin Hall conductivity as well as band-resolved and k -resolved spin Berry curvatures. As LaAlSi and LaAlGe have very similar geometric and electronic structures, we particularly take LaAlGe as an example in the discussion. In the [Sec.III E](#), we calculate the electrical conductivity through the Boltzmann transport equation with the EPW approach, and then evaluate the spin Hall angles. We finally summarize our work and draw conclusions in [Sec.IV](#).

II. METHODOLOGY

Our first-principles calculations were performed using the QUANTUM ESPRESSO package [38, 39]. A plane wave basis was used and the pseudopotential was from PSLIBRARY [40]. We used a fully relativistic pseudopotential with the generalized gradient approximation (GGA) based on the projector wave augmented (PAW) method with a Perdew-Burke-Ernzerhof (PBE) functional. The Hubbard energy U of 4 eV was used for La in our calculations. The plane-wave and charge density cutoff energy is 75 Ry and 750 Ry, respectively. A k -point

grid of $8 \times 8 \times 8$ was used in the self-consistent calculations. All structures were fully relaxed with the force on each atom was less than 10^{-3} Ry/Bohr. Spin-orbit interaction was taken into account self-consistently to treat the relativistic effects. Once the self-consistent calculations were completed, the Bloch functions were Fourier transformed to the maximally localized Wannier functions (MLWFs) using the WANNIER90 package [41]. The SHC was calculated using the BERRY module on a dense $120 \times 120 \times 120$ k -mesh. Since the spin Berry curvature has rapid variations, adaptive smearing was used.

The intrinsic SHC was calculated via the Kubo formula, as shown below, in the clean limit. We expect the SHC in the clean limit to be given by the intrinsic SHC value due to the vanishing vertex corrections under the symmetry of $H(\mathbf{k}) = H(-\mathbf{k})$ [20, 42–44].

$$\sigma_{xy}^z = e\hbar \int_{BZ} \frac{d\mathbf{k}}{(2\pi)^3} \sum_n f_{n\mathbf{k}} \Omega_{xy}^{n,z}(\mathbf{k}), \quad (1)$$

where, $f_{n\mathbf{k}}$ is the Fermi-Dirac distribution function for the n th band at \mathbf{k} , which includes the temperature dependency of SHC. The SHC tensor element σ_{xy}^z describes the spin current J_x with spin polarization along z direction due to an incoming charge current from the y direction. Other elements in the third-order tensor can be obtained by changing the mutually orthogonal Cartesian directions. $\Omega_{xy}^{n,z}(\mathbf{k})$ is the Berry curvature of the n th band as:

$$\Omega_{xy}^{n,z}(\mathbf{k}) = - \sum_{m \neq n} \frac{2\text{Im}[\langle n\mathbf{k} | j_x^z | m\mathbf{k} \rangle \langle m\mathbf{k} | v_y | n\mathbf{k} \rangle]}{(\epsilon_{n\mathbf{k}} - \epsilon_{m\mathbf{k}})^2} \quad (2)$$

where j_x^z and v_y is the spin current operator and the velocity operator.

In order to evaluate the electrical conductivity, the energy and k -point dependent carrier relaxation time is calculated by utilizing electron-phonon Wannier (EPW) packages [45]. The scattering of electrons from the acoustic and optical phonon have been accounted for. The electron energy is computed on a $6 \times 6 \times 6$ k -point mesh and the phonon dispersion is obtained using density functional perturbation (DFPT) method on an $3 \times 3 \times 3$ q -point grid. Subsequently, the electron-phonon matrix elements and the imaginary part of self-energies $\Im(\Sigma_{nk})$ corresponding to the eigenvalues E_{nk} are obtained for each electronic state of the n^{th} band and the k momentum. The relaxation time τ_{nk} associated with the electron-phonon

interaction for each electronic state can be extracted by the formula:

$$\tau_{nk}^{-1} = \frac{2}{\hbar} \text{Im}(\sum_{nk}) = \frac{2\pi}{\hbar} \sum_m \int_{BZ} \frac{dq}{\Omega_{BZ}} |g_{mn}(k, q)|^2 \quad (3)$$

$$\{[(n_q + f_{m,k+q})\delta(E_{m,k+q} - E_{n,k} - \hbar\omega_q)] + [(1 + n_q - f_{m,k+q})\delta(E_{m,k+q} - E_{n,k} - \hbar\omega_q)]\}$$

where $g_{mn}(k, q)$ is the element of the electron-phonon coupling matrix, m and n are band index, k and q are wave vectors of the initial electronic states and phonon states, E_{mk} and $\hbar\omega_q$ are energies of electrons and phones with f_{mk} and n_q being their distribution functions, respectively. Using the eigenvalue and the carrier relaxation time, the electronic conductivity (σ) are evaluated by utilizing the Boltzmann transport theory within the constant relaxation time approximation.

III. RESULTS AND DISCUSSION

A. Geometrical structures

Both LaAlSi and LaAlGe have the same crystal structure, which is in a body-centered tetragonal Bravais lattice with nonsymmorphic space group $I4_1md$ (no. 109), C_{4v} point group, lacking inversion symmetry (\mathcal{I}) as shown in **Figure 1**. The conventional cell consists of 12 atomic layers along the (001) direction, each of which contains only one type of elements (**Fig. 1a**). The x , y and z are directions along the crystal lattice of a , b and c , respectively. The lattice constants are $a = b = 4.325\text{\AA}$ and $c = 17.745\text{\AA}$ for LaAlSi while $a = b = 4.371\text{\AA}$ and $c = 14.849\text{\AA}$ for LaAlGe. The conventional cell possesses two pure mirror symmetries (M_x and M_y) and two glide-mirror symmetries (M_{xy} and M_{x-y}). Because of these symmetries, only $\{m_{010}|0\}$ and $\{m_{110}|0\frac{1}{2}\frac{1}{4}\}$ are associated with a translation by $b/2$ and $c/4$ are shown in **Figs. 1b, 1c**. The C_2 rotational axis can be found in the top view of **Fig. 1d**. The Brillouin zone (BZ) of the bulk and (001) surface with the M_y and M_{xy} mirror planes (**Fig. 1e**). The orange plane, which is spanned by Γ , Σ , N , Σ_1 and Z points, is invariant under the mirror reflection M_y . The turquoise green plane, which is spanned by Γ , X and Z points, is invariant under the mirror reflection M_{xy} .

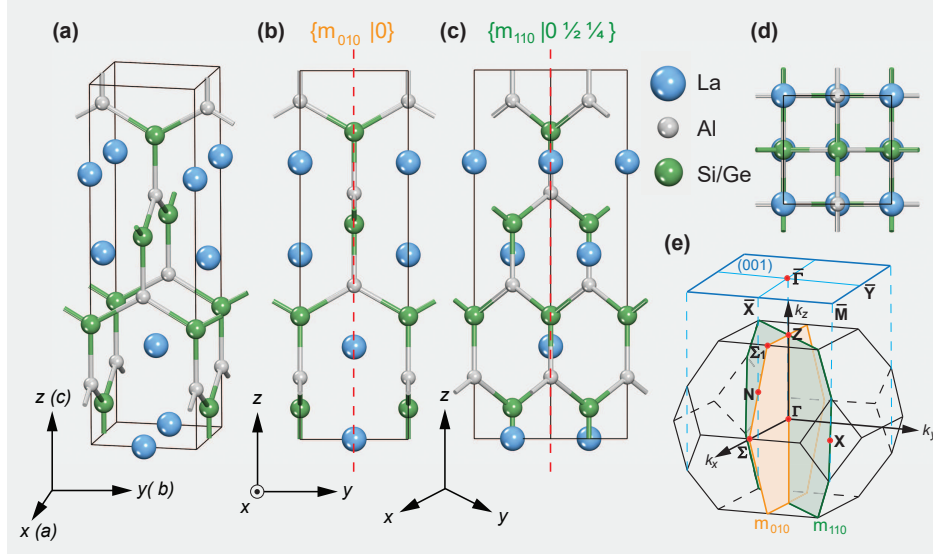


FIG. 1: Crystal structures and Brillouin zone of LaAlX (X=Si, Ge). (a) Conventional body-centered tetragonal structure of LaAlX with nonsymmorphic space group $I4_1md$ (109) and C_{4v} point group. x , y and z are directions along the crystal lattice of a , b and c , respectively. The conventional cell possesses two pure mirror symmetries (M_x and M_y) and two glide-mirror symmetries (M_{xy} and M_{x-y}). Because of these symmetries, only $\{m_{010}|0\}$ and $\{m_{110}|0 \frac{1}{2} \frac{1}{4}\}$ in (b) and (c). (d) The top view of crystal. (e) The Brillouin zone of the bulk and (001) surface with the M_y and M_{xy} mirror planes. The orange and turquoise green plane is invariant under mirror M_y and M_{xy} .

B. Electronic band structures

Our band structure calculations of LaAlSi and LaAlGe without SOC are shown in [Figures 2a, 2b](#). It can be seen that the conduction and valence bands cross each other along the $\Gamma - \Sigma - \Sigma_1$ path. Such Dirac-like crossings demonstrate that LaAlSi and LaAlGe are semimetals, which is in good agreement with previous reports [32, 34, 37]. It is interesting to notice the existence of two types of Weyl points, i.e., type-I and type-II. The latter is highlighted in the shaded orange box, which can be further confirmed by the calculated Fermi surface over the first bulk Brillouin zone in [Figs. 2c, 2d](#). The electron- and hole-like pockets are shown in magenta and cyan colours from the Weyl cones. The e-h touching in the Fermi surface (in the shaded orange box) confirms the type-II nature of crossing in the band structure. Furthermore, we highlight a crossing along the Γ - X path using a green box,

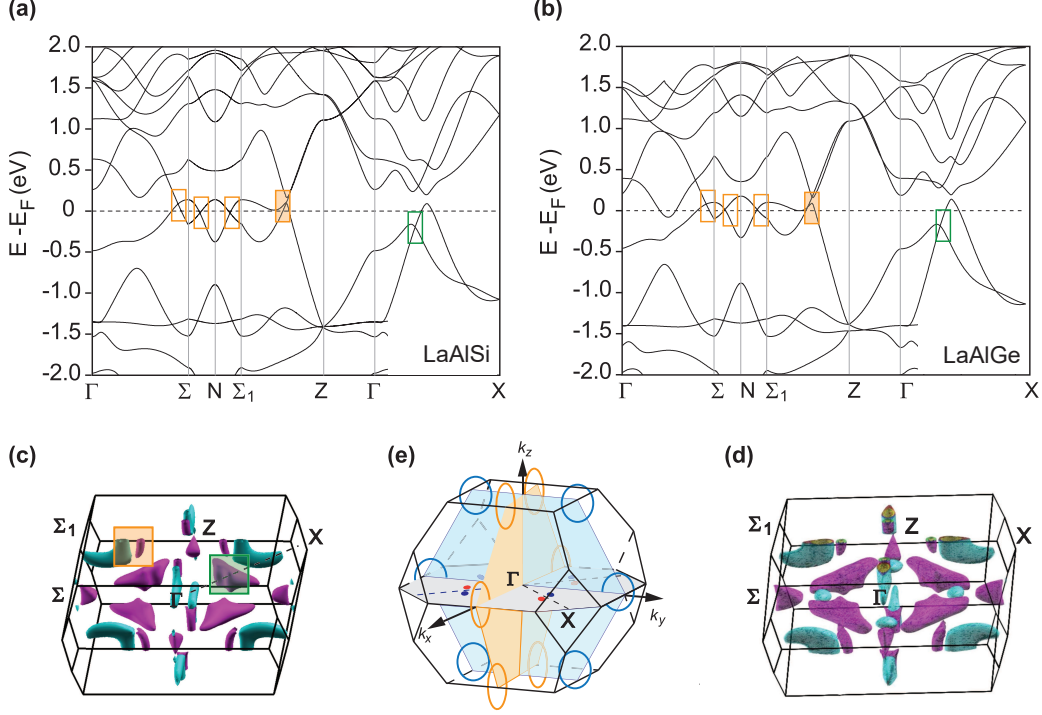


FIG. 2: Band structures and the Fermi surfaces of LaAlSi and LaAlGe. (a) and (b) are band structures of LaAlSi and LaAlGe along the high-symmetry directions without SOC. Multiple Dirac-like crossings are visible near the Fermi level along the Γ - Σ - N - Σ_1 - Z lines within the M_y mirror plane, and along the Γ - X - Z lines in the M_{xy} mirror plane. The crossing in the shaded orange box is a type-II Weyl node. (c) and (d) are Fermi surfaces of LaAlSi and LaAlGe over the bulk Brillouin zone. The electron- and hole-like pockets are shown in magenta and cyan colours. These band crossings form two pairs of “nodal rings” in the two mirror planes, M_x and M_y in (e). Furthermore, four pairs of “nodal points” are labelled by red and blue dots in the $k_z = 0$ plane along Γ - X and in the vicinity of the glide-mirror planes.

the anticrossing of this point contributes to the maximum spin Hall conductivity, which will be discussed in details in the next Section. The Dirac-like crossings near to E_F are mainly along the Γ - Σ - N - Σ_1 - Z lines and the Γ - X - Z lines. The plane spanned by the Γ , N , and Z points is invariant under the mirror reflection M_y , and the energy bands within this plane can be labelled by the mirror eigenvalues ± 1 [26]. The symmetry analysis in previous report[32] shows that the two bands that cross along the Γ - Σ - N - Σ_1 - Z path belong to opposite mirror eigenvalues, and hence, the crossings between them (labelled by orange rectangles) are protected by the mirror symmetry. A similar band crossing can be found

along Γ -X line in the ΓXZ plane. Together, these band crossing points form two pairs of “nodal rings” in the two mirror planes and four pairs of “nodal points” (Fig. 2e). In this paper, we specially focus on the spin Hall effect in LaAlSi and LaAlGe. The detailed discussion on the Weyl features of these two materials can be found in previous computational and experimental works [32–37].

C. Spin Hall conductivity

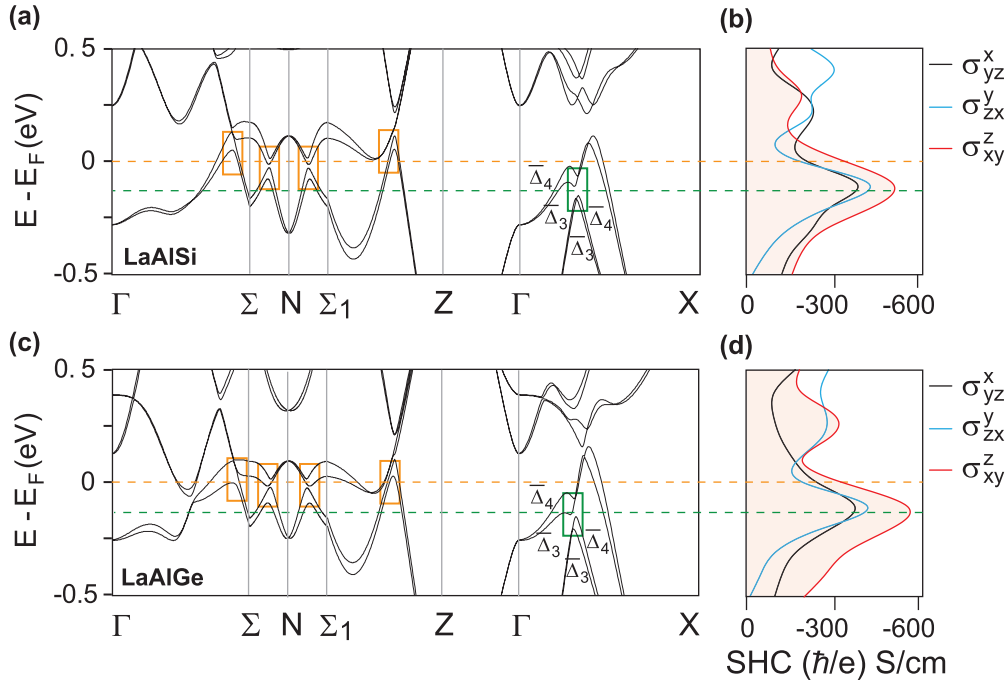


FIG. 3: Relativistic band structures and spin Hall conductivities as a function of the energy of LaAlSi and LaAlGe. The Fermi level is set to zero, indicated by the orange dashed line. The green dashed line shows the position of 0.12 eV below the Fermi level. (a) and (c) The band structures of LaAlSi and LaAlGe in the presence of SOC which opens full gaps in the mirror planes because of the identical irreps ($\bar{\Delta}_3$ and $\bar{\Delta}_4$) of those Dirac-like cones. These anticrossings contribute significantly to the spin Hall conductivity. (b) and (d) The energy dependency of SHC of 3 nonzero tensor elements. The maximum SHC is marked by the green dashed line.

In Sections III A, III B, we have discussed that LaAlSi and LaAlGe have 4 mirror planes and 4 other symmetry operations, such high symmetries generate multiple Dirac-like cones

near E_F along particular directions (forming nodal lines) or at specific points (forming nodal points). Unlike Dirac surface states in topological insulators, some robust Dirac-like points in Weyl semimetals are protected by one or more crystalline symmetries, while some are unprotected. These protected Dirac-like cones are robust against the SOC from being gapped out, such as the crossing that is described by C_{2v} point group with four irreducible representations. However, those unprotected crossings would be gapped by the SOC because their “accidental” crossings belong to the point groups with only one irreducible representation. Compared to searching for topological materials with topologically protected gapless Dirac-like cones, one should focus on the presence of capped crossings for discovering spin Hall materials. It is because the sign of the spin berry curvature (SBC) is opposite on either side of the gap, which cannot be cancelled out if the Fermi level is in or very close to the gap. Such gaped nodal lines/points generate large spin Hall conductivity as the intrinsic SHC is proportional to the integration of the SBC of occupied bands.

In this Section, we first check how the Dirac-like crossings in the band structure (**Figures 2a and 2b**) undergo in the presence of SOC, and then calculate SHC of LaAlSi and LaAlGe. **Figure 3a** shows the band structure of LaAlSi with SOC. As shown, most Dirac-like cones, highlighted by rectangular boxes, are gapped out by SOC, which indicates that the nodal lines have disappeared in the absence of SOC. Taking the gap along Γ -X in the green box as an example, we analyse the groups of bands to understand the origin of such gapping by SOC. As can be seen in **Fig. 3a**, the original crossing of two bands with identical irreps $\overline{\Delta}_3$ and $\overline{\Delta}_4$, respectively, of little group C_5 , which means SOC will gap this non-orthogonal nodal point and give rise to a non-vanishing energy term when two bands hybridize. These opened gaps near the Fermi level contribute significantly to the spin Hall conductivity. LaAlGe has the similar SOC-induced gapping features in the band structure (**Fig. 3c**), and we thus expect that both of them may have large SHC according to their anticrossing features near E_F .

It is worth to note that the SHC of LaAlX is anisotropic on the basis of the linear response due to their tetragonal lattice with \mathcal{I} -breaking. Other existing symmetries, such as mirror reflections and \mathcal{T} , force some tensor elements to be zero or equivalent. Thus, LaAlX only have three sets of nonzero elements $\sigma_{xy}^z = -\sigma_{yx}^z$, $\sigma_{zx}^y = -\sigma_{zy}^y$, and $\sigma_{yz}^x = -\sigma_{xz}^x$. **Figures 3b, 3d** show the energy dependence of the SHC of 3 nonzero tensor elements of LaAlSi and LaAlGe. As shown, they indeed have large SHC when the chemical potential is zero

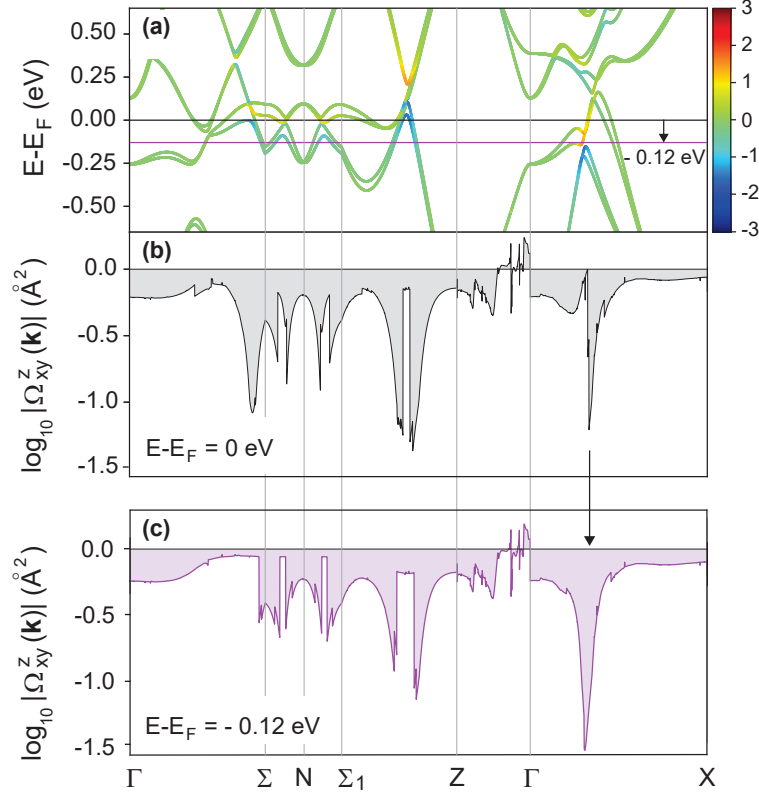


FIG. 4: The band structure projected by spin Berry curvature of LaAlGe and the k -resolved spin Berry curvatures of Ω_{xy}^z on a log scale. (a) The SBC-projected band structure, where the red (blue) colour denotes a positive (negative) contribution of the spin Berry curvature. The solid black line and dotted purple line labels the chemical potential $\Delta\mu = 0$ eV and $\Delta\mu = -0.12$ eV, respectively. (b) and (c) k -resolved SBC along the same high-symmetry paths, at $E = E_F$ and $E = E_F - 0.12$ eV. A significant enhancement of the SBC peak in the Γ -X segment is indicated by an arrow.

($\Delta\mu = 0$ eV). This is summarized in [Table I](#) and compared with Pt [21, 46] and some typical type-II Weyl semimetals [3, 14, 22, 47]. The values of the SHC are robust as all 3 tensor elements are more than $-200(\hbar/e)$ S/cm, while other type-II Weyl semimetals, such as WTe₂, only have a large SHC along a particular direction (see in [Table I](#)). Such strong dependence on the sample orientation for the SHE poses a challenge in experiments, and might be the reason of the large experimentally reported variation of spin Hall angles (0.029–0.5) in WTe₂ [3, 14, 31]. Remarkably, the SHC reaches its maximum value when E_F

lies in the gap along the Γ - X path ($\Delta\mu = 0.12$ eV). Furthermore, the SHC_{max} of LaAlGe (such as $\sigma_{xy}^z = -560$ (\hbar/e) S/cm) is slightly higher than that of LaAlSi (-523 (\hbar/e) S/cm) because LaAlGe has a small gap in the green box. All these results demonstrate that 1) the anticrossings by SOC in the bulk band structure are the sources of the large SHC; 2) the SHC originates from the SOC-driven gap, but its magnitude is inversely proportional to the size of the gap; and 3) the SHC can be further tuned by changing the chemical potential, such as the application of an external electric field or doping of holes.

TABLE I: SHC tensor elements at the Fermi energy level ($\Delta\mu = 0$ eV, $T = 0$ K) in units of (\hbar/e) S/cm, electrical conductivities in units of S/cm, and dimensionless spin Hall angles. The values in the brackets are at 300 K.

Material	σ_{yz}^x	σ_{zx}^y	σ_{xy}^z	SHC (exp.)	electrical conductivity	$ \theta_{SH} $	Reference
Pt (cal.)			2139				Ref.[46]
Pt (cal.)			2050				this work
Pt (exp.)				1900	5×10^4	0.068	Ref.[21]
MoTe ₂ (cal.)	-18	286	-176				Ref.[22]
MoTe ₂ (exp.)				29	1.8×10^3	0.032	Ref.[47]
WTe ₂ (cal.)	-44	103	-204				Ref.[22]
WTe ₂ (cal.)	14	96			1.13×10^3		Ref.[31]
WTe ₂ (cal.)	-35		-247				this work
WTe ₂ (exp.)				40	2.6×10^3	0.029	Ref.[14]
WTe ₂ (exp.)				20-300	$1.4\text{-}1.7 \times 10^3$	0.09-0.5	Ref.[3]
LaAlSi	-235 (-265)	-202 (-228)	-336 (-355)		1.72×10^4	0.04	this work
LaAlGe	-257 (-273)	-214 (-239)	-351 (-370)		1.25×10^4	0.06	this work

D. Spin Berry curvature

In order to understand the physics of the large SHC in LaAlX and its enhancement through hole doping (shifting E_F downward by 0.12 eV) in **Figs. 3b, 3d**, we take σ_{xy}^z of LaAlGe as an example where its spin Berry curvature is projected onto its band structure

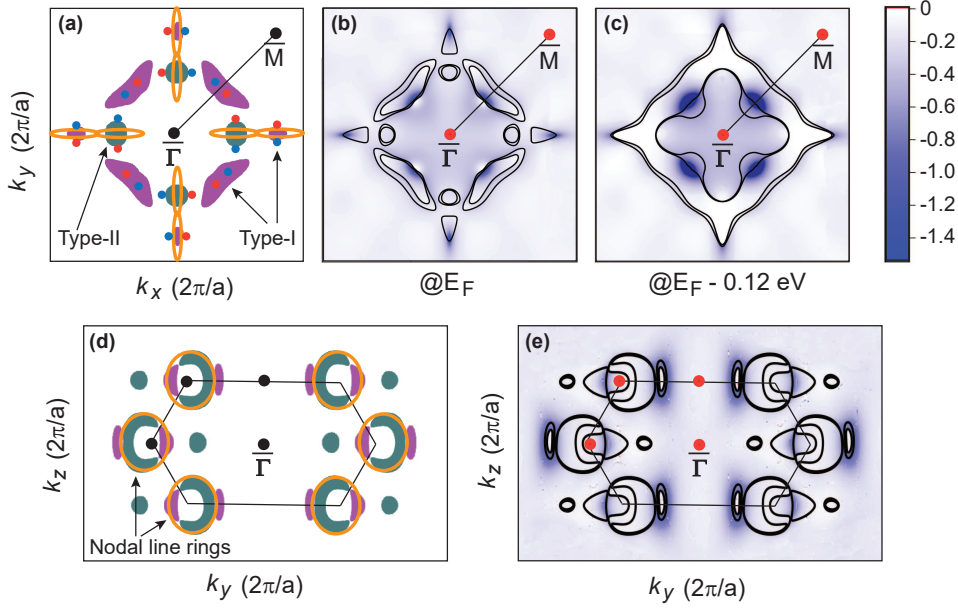


FIG. 5: Projected Fermi surfaces and k -resolved spin Berry curvatures on a log scale in k_x - k_y and k_y - k_z planes in the BZ for σ_{xy}^z SHC of LaAlGe. (a) The k_x - k_y Fermi surface map at $k_z = 0$ in Brillouin zone. The nodal rings are highlighted by orange rings. The Weyl nodal points are labelled by red/blue dots with different chirality. (b) and (c) k -resolved spin Berry curvatures in the 2D BZ ($k_z = 0$) at E_F and $E_F - 0.12$ eV. (d) The k_y - k_z Fermi surface map at $k_x = 0$ in the region of BZ. The orange loops indicate a pair of nodal lines which are on the k_y - k_z plane, protected by the mirror symmetry. (e) The k -resolved SBC ($k_x = 0$) at E_F . The dominate amplitude of the spin Berry curvature (blue regions) is distributed mainly around the areas of nodal lines/points.

(Fig. 4a) and plot its k -resolved spin Berry curvatures at $E = E_F$ and $E = E_F - 0.12$ eV (Figs. 4b, 4c). It is known that the spin Berry curvature, that is a part of a broader concept arising from the k -dependence of the wave function, is heavily influenced by the orbital hybridization and the position of E_F in the electronic band structure. Figure 4a shows the SBC-projected band structure, in which the red (blue) colour denotes a positive (negative) contribution of the spin Berry curvature. As shown, there are several gaps near to E_F along the Γ -N-Z lines in the Brillouin zone. Most sharp peaks in the k -resolved SBC (Fig. 4b) correspond to these gaps. Thus, it is clear that the bands close to E_F at the SOC-induced gapping points mainly contribute to spin Hall conductivity. This is because

the unoccupied bands below the E_F contribute largely to the SBC. After lowering the Fermi energy by 0.12 eV from charge neutral point ($\Delta\mu = 0$ eV), the Fermi energy passes through another SOC gap along the Γ - X path. From the k -resolved spin Berry curvature in **Fig. 4c**, one can see a significant enhancement of the SBC peak between Γ and X , resulting in an overall increase of SHC.

The origin of the large SBC from the gapped nodal lines/points and the increasing trend of the SBC with the shift of E_F can be seen more clearly from the k -resolved spin Berry curvature in the 2D Brillouin zone. **Figures 5a and 5d** show the 2D Fermi surface projected on the k_x - k_y ($k_z = 0$) and k_y - k_z ($k_x = 0$) plane. One can see that there are four pairs of nodal rings with two in each plane. Furthermore, a pair of nodal points are near the diagonal Γ - M line. Next, let's compare the k -resolved Fermi surface with the k -resolved spin Berry curvature projected onto the same plane. As clearly shown from **Figs. 5a, 5b or 5d, 5e**, the large SBC magnitude are located in the proximity of the nodal lines/points which are gapped out by SOC. Furthermore, there is a significant enhancement of the SBC around the nodal points along Γ - M when E_F is shifted to -0.12 eV by comparing **Fig. 5b** with **Fig. 5c**. The above analysis clarifies the mechanism of the SHC variation with the position of E_F , and sheds light on an effective approach to optimize the SHC in spin Hall materials.

E. Spin Hall angle

In order to determine the spin Hall angle with σ_{xy}^z , we calculate the longitudinal electrical conductivity σ_{xx} using the Boltzmann transport equation within the constant relaxation time approximation [48]. The relaxation time was calculated using the electron-phonon Wannier method. Here, we consider two conditions, tuning the chemical potential and increasing the temperature. It is worth noting that the shifting of E_F is converted into the change of the hole concentration in the calculation of electrical conductivity. We assume that a low hole doping concentration does not change the electronic band structure by much and only lowers E_F slightly. The calculated hole-doping and temperature dependence of spin Hall angles of LaAlGe are shown in **Fig. 6a**. As can be seen, the SHA is increases linearly with the increase in temperature. This is due to the temperature dependent changes of the SHC and electrical conductivity as shown in **Fig. 6b**. The numerator σ_{SH} (denominator

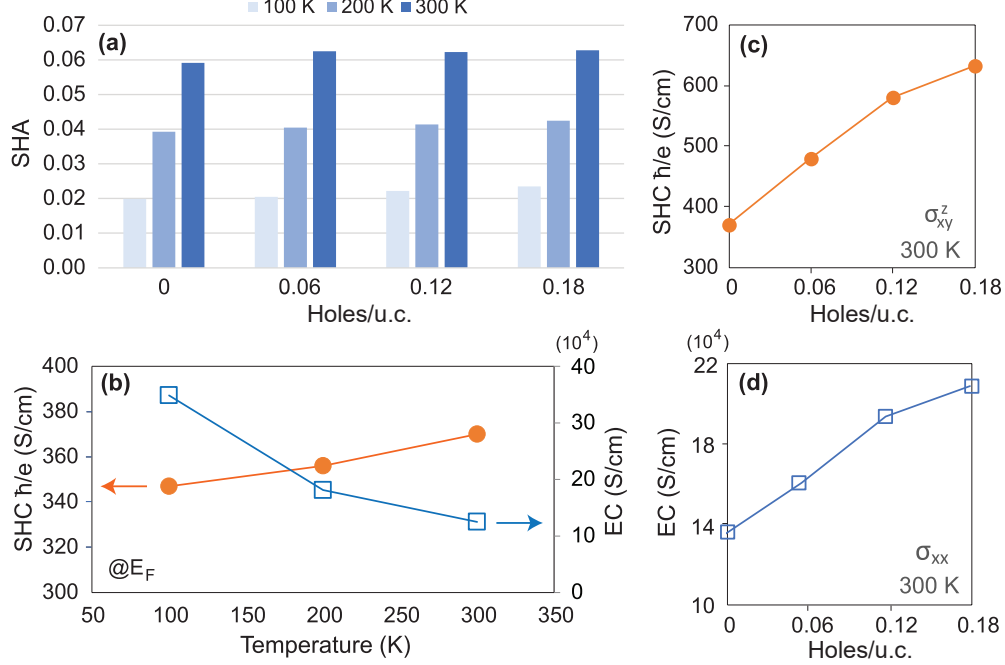


FIG. 6: (a) The calculated chemical potential and temperature dependence of spin Hall angles of LaAlGe. (b) The temperature dependence of spin Hall conductivity (orange) and electrical conductivity (blue) at the Fermi level ($E - E_F = 0$). (c) and (d) The chemical potential dependence of spin Hall conductivity and electrical conductivity at 300 K.

σ_c) is increasing (decreasing) with the increase of temperature, resulting in the increase of the quotient θ_{SH} with a 300% enhancement of σ_{SH} from 100 K to room temperature. The increase of SHC with the increase of temperature can be understood by the calculated SHC near E_F in **Fig.3d**. As shown, the Fermi level is close to the peak of SHC in LaAlGe. The smearing of the temperature will cover more states of the SHC from the peak. For comparison, the E_F is located at the peak of SHC of TaAs [23], the increase in temperature will cover less states, resulting in a decrease of the SHC [23]. In addition, it is found that the change of E_F is an effective approach to enhance the SHC (**Fig.6c** and Sec.III C). However, it will not increase the spin Hall angle due to the simultaneous increase of the electrical conductivity (**Fig.6d**). LaAlGe has a slightly larger spin Hall conductivity and smaller electrical conductivity than LaAlSi in the charge neutral case. The small charge current required in LaAlGe leads to lower Joule heating for the generation of the same amount of spin Hall current. Overall, LaAlGe has 50% higher SHA compared with LaAlSi (see in

Table I).

IV. CONCLUSIONS

In summary, we systematically study the electronic structure, spin Hall effect, and spin Hall angle of a family of type-II Weyl semimetals, LaAlSi and LaAlGe, using the first-principles calculations with the Berry phase formalism and electron-phonon Wannier method. Both of them have large spin Hall conductivity which can be further increased by tuning the chemical potential downwards (i.e., hole doping). We reveal the physical origin of their strong SHE, which is from the high mirror symmetry and large SOC. The former gives rise to many Dirac-like crossings near the Fermi energy level, but are unprotected against SOC, resulting in anticrossings in the presence of SOC. These SOC-gapped nodal lines/points near E_F create a highly unbalanced spin Berry curvature integral, and thus large spin Hall conductivity. The spin Hall conductivity can be increased by slightly tuning the Fermi level within other small gaps in the Brillouin zone. Remarkably, our results show that increasing the temperature can boost the SHC while suppressing the electrical conductivity, which enhances the spin Hall angle and the spin-orbit torque efficiency. The strong SHE can generate spin accumulation at two surfaces, which leads to unique effects in the unidirectional spin Hall magnetoresistance in FM/WSM heterostructures. The strong SHE also can be used to electrically generate spin currents and switch the magnetization of ferromagnets in spin-orbitronics applications. Furthermore, the high values of the intrinsic SHC and SHA of LaAlX could be retained and/or enhanced at room temperature, offering a great advantage for devices operated under room-temperature.

V. ACKNOWLEDGEMENTS

The Authors thank Dr. Jun Zhou his for helpful discussion. K.T., H.Y. and L.S. thank MOE Tier 1 group grant (R-263-000-D60-114,R-263-000-D61-114 and R-265-000-651-114).

The calculations were carried out on the GRC-NUS high-performance computing facilities.

- [1] N. Sato, F. Xue, R. M. White, C. Bi, and S. X. Wang, Two-terminal spin-orbit torque magnetoresistive random access memory, *Nat. Electron.* **1**, 508 (2018).
- [2] Y. Wang, D. Zhu, Y. Yang, K. Lee, R. Mishra, G. Go, S.-H. Oh, D.-H. Kim, K. Cai, E. Liu, *et al.*, Magnetization switching by magnon-mediated spin torque through an antiferromagnetic insulator, *Science* **366**, 1125 (2019).
- [3] S. Shi, S. Liang, Z. Zhu, K. Cai, S. D. Pollard, Y. Wang, J. Wang, Q. Wang, P. He, J. Yu, *et al.*, All-electric magnetization switching and Dzyaloshinskii–Moriya interaction in WTe₂/ferromagnet heterostructures, *Nat. Nanotechnol.* **14**, 945 (2019).
- [4] R. Mishra, F. Mahfouzi, D. Kumar, K. Cai, M. Chen, X. Qiu, N. Kioussis, and H. Yang, Electric-field control of spin accumulation direction for spin-orbit torques, *Nat. Commun.* **10**, 1 (2019).
- [5] Z. Luo, Q. Zhang, Y. Xu, Y. Yang, X. Zhang, and Y. Wu, Spin-orbit torque in a single ferromagnetic layer induced by surface spin rotation, *Phys. Rev. Appl.* **11**, 064021 (2019).
- [6] Y. Liu, A. P. Chen, L. Ren, Y. Liu, S. Srivastava, H. Yang, Y. P. Feng, and K. L. Teo, Engineering interfacial perpendicular magnetic anisotropy in Fe₂CoSi/Pt multilayers with interfacial strain and orbital hybridization, *ACS Appl. Electron. Mater.* **1**, 1251 (2019).
- [7] K. Cai, Z. Zhu, J. M. Lee, R. Mishra, L. Ren, S. D. Pollard, P. He, G. Liang, K. L. Teo, and H. Yang, Ultrafast and energy-efficient spin-orbit torque switching in compensated ferrimagnets, *Nat. Electron.* **3**, 37 (2020).
- [8] I. M. Miron, K. Garello, G. Gaudin, P.-J. Zermatten, M. V. Costache, S. Auffret, S. Bandiera, B. Rodmacq, A. Schuhl, and P. Gambardella, Perpendicular switching of a single ferromagnetic layer induced by in-plane current injection, *Nature* **476**, 189 (2011).
- [9] L. Liu, C.-F. Pai, Y. Li, H. Tseng, D. Ralph, and R. Buhrman, Spin-torque switching with the giant spin hall effect of tantalum, *Science* **336**, 555 (2012).
- [10] A. Manchon, J. Železný, I. M. Miron, T. Jungwirth, J. Sinova, A. Thiaville, K. Garello, and P. Gambardella, Current-induced spin-orbit torques in ferromagnetic and antiferromagnetic systems, *Reviews of Modern Physics* **91**, 035004 (2019).

- [11] Y. Xu, Y. Yang, Z. Luo, and Y. Wu, Disentangling magnon magnetoresistance from anisotropic and spin Hall magnetoresistance in NiFe/Pt bilayers, *Phys. Rev. B* **100**, 094413 (2019).
- [12] Y. Zhang, Y. Sun, H. Yang, J. Zelezny, S. P. Parkin, C. Felser, and B. Yan, Strong anisotropic anomalous hall effect and spin hall effect in the chiral antiferromagnetic compounds Mn_3X ($X= Ge, Sn, Ga, Ir, Rh,$ and Pt), *Phys. Rev. B* **95**, 075128 (2017).
- [13] P. Song, C.-H. Hsu, G. Vignale, M. Zhao, J. Liu, Y. Deng, W. Fu, Y. Liu, Y. Zhang, H. Lin, *et al.*, Coexistence of large conventional and planar spin Hall effect with long spin diffusion length in a low-symmetry semimetal at room temperature, *Nat. Mater.* **19**, 292 (2020).
- [14] D. MacNeill, G. Stiehl, M. Guimaraes, R. Buhrman, J. Park, and D. Ralph, Control of spin-orbit torques through crystal symmetry in WTe_2 /ferromagnet bilayers, *Nat. Phys.* **13**, 300 (2017).
- [15] H. Xu, J. Wei, H. Zhou, J. Feng, T. Xu, H. Du, C. He, Y. Huang, J. Zhang, Y. Liu, *et al.*, High spin Hall conductivity in large-area type-II Dirac semimetal $PtTe_2$, *Adv. Mater.* **32**, 2000513 (2020).
- [16] S. Shi, A. Wang, Y. Wang, R. Ramaswamy, L. Shen, J. Moon, D. Zhu, J. Yu, S. Oh, Y. Feng, *et al.*, Efficient charge-spin conversion and magnetization switching through the Rashba effect at topological-insulator/Ag interfaces, *Phys. Rev. B* **97**, 041115 (2018).
- [17] Y. Wang, P. Deorani, K. Banerjee, N. Koirala, M. Brahlek, S. Oh, and H. Yang, Topological surface states originated spin-orbit torques in Bi_2Se_3 , *Phys. Rev. Lett.* **114**, 257202 (2015).
- [18] F. Mahfouzi, R. Mishra, P.-H. Chang, H. Yang, and N. Kioussis, Microscopic origin of spin-orbit torque in ferromagnetic heterostructures: A first-principles approach, *Phys. Rev. B* **101**, 060405 (2020).
- [19] X. Sui, C. Wang, J. Kim, J. Wang, S. Rhim, W. Duan, and N. Kioussis, Giant enhancement of the intrinsic spin hall conductivity in β -tungsten via substitutional doping, *Phys. Rev. B* **96**, 241105 (2017).
- [20] J. Qiao, J. Zhou, Z. Yuan, and W. Zhao, Calculation of intrinsic spin Hall conductivity by Wannier interpolation, *Phys. Rev. B* **98**, 214402 (2018).
- [21] Y. Wang, P. Deorani, X. Qiu, J. H. Kwon, and H. Yang, Determination of intrinsic spin Hall angle in Pt, *Appl. Phys. Lett.* **105**, 152412 (2014).
- [22] J. Zhou, J. Qiao, A. Bournel, and W. Zhao, Intrinsic spin Hall conductivity of $MoTe_2$ and WTe_2 semimetals, *Phys. Rev. B* **99**, 060408 (2019).

- [23] Y. Sun, Y. Zhang, C. Felser, and B. Yan, Strong intrinsic spin hall effect in the TaAs family of Weyl semimetals, *Phys. Rev. Lett.* **117**, 146403 (2016).
- [24] Y. Fan, P. Upadhyaya, X. Kou, M. Lang, S. Takei, Z. Wang, J. Tang, L. He, L.-T. Chang, M. Montazeri, *et al.*, Magnetization switching through giant spin-orbit torque in a magnetically doped topological insulator heterostructure, *Nat. Mater.* **13**, 699 (2014).
- [25] Y. Shiomi, K. Nomura, Y. Kajiwara, K. Eto, M. Novak, K. Segawa, Y. Ando, and E. Saitoh, Spin-electricity conversion induced by spin injection into topological insulators, *Phys. Rev. Lett.* **113**, 196601 (2014).
- [26] H. Weng, C. Fang, Z. Fang, B. A. Bernevig, and X. Dai, Weyl semimetal phase in noncentrosymmetric transition-metal monophosphides, *Phys. Rev. X* **5**, 011029 (2015).
- [27] A. A. Soluyanov, D. Gresch, Z. Wang, Q. Wu, M. Troyer, X. Dai, and B. A. Bernevig, Type-II Weyl semimetals, *Nature* **527**, 495 (2015).
- [28] Y. Sun, Y. Zhang, C.-X. Liu, C. Felser, B. Yan, Y. Sun, Y. Zhang, C.-X. Liu, C. Felser, and B. Yan, Dirac nodal lines and induced spin Hall effect in metallic rutile oxides, *Phys. Rev. B* **95**, 235104 (2017).
- [29] E. Derunova, Y. Sun, C. Felser, S. S. P. Parkin, B. Yan, and M. N. Ali, Giant intrinsic spin hall effect in W_3Ta and other A15 superconductors, *Comput. Mater. Sci.* **5**, eaav8575 (2019).
- [30] Y. Yen and G.-Y. Guo, Tunable large spin Hall and spin Nernst effects in the Dirac semimetals $ZrXY$ ($X = Si, Ge$; $Y = S, Se, Te$), *Phys. Rev. B* **101**, 064430 (2020).
- [31] B. Zhao, D. Khokhriakov, Y. Zhang, H. Fu, B. Karpiak, A. M. Hoque, X. Xu, Y. Jiang, B. Yan, and S. P. Dash, Observation of spin hall effect in Weyl semimetal WTe_2 at room temperature, *Phys. Rev. Research* **2**, 013286 (2020).
- [32] G. Chang, B. Singh, S.-Y. Xu, G. Bian, S.-M. Huang, C.-H. Hsu, I. Belopolski, N. Alidoust, D. S. Sanchez, H. Zheng, *et al.*, Magnetic and noncentrosymmetric Weyl fermion semimetals in the $RAlGe$ family of compounds ($R = \text{rare earth}$), *Phys. Rev. B* **97**, 041104 (2018).
- [33] D. Destratz, L. Das, S. S. Tsirkin, Y. Xu, T. Neupert, J. Chang, A. Schilling, A. G. Grushin, J. Kohlbrecher, L. Keller, *et al.*, Magnetism and anomalous transport in the Weyl semimetal $PrAlGe$: possible route to axial gauge fields, *npj Quantum Mater.* **5**, 1 (2020).
- [34] H. Hodovanets, C. Eckberg, P. Zavalij, H. Kim, W.-C. Lin, M. Zic, D. Campbell, J. Higgins, and J. Paglione, Single-crystal investigation of the proposed type-II Weyl semimetal $CeAlGe$, *Phys. Rev. B* **98**, 245132 (2018).

- [35] M. Lyu, J. Xiang, Z. Mi, H. Zhao, Z. Wang, E. Liu, G. Chen, Z. Ren, G. Li, and P. Sun, Nonsaturating magnetoresistance, anomalous Hall effect, and magnetic quantum oscillations in ferromagnetic semimetal PrAlSi, arXiv preprint arXiv:2001.05398.
- [36] P. Puphal, V. Pomjakushin, N. Kanazawa, V. Ukleev, D. J. Gawryluk, J. Ma, M. Naamneh, N. C. Plumb, L. Keller, R. Cubitt, *et al.*, Topological magnetic phase in the candidate Weyl semimetal CeAlGe, Phys. Rev. Lett. **124**, 017202 (2020).
- [37] S.-Y. Xu, N. Alidoust, G. Chang, H. Lu, B. Singh, I. Belopolski, D. S. Sanchez, X. Zhang, G. Bian, H. Zheng, *et al.*, Discovery of Lorentz-violating type-II Weyl fermions in LaAlGe, Sci. Adv. **3**, e1603266 (2017).
- [38] P. Giannozzi, S. Baroni, N. Bonini, M. Calandra, R. Car, C. Cavazzoni, D. Ceresoli, G. L. Chiarotti, M. Cococcioni, I. Dabo, *et al.*, QUANTUM ESPRESSO: a modular and open-source software project for quantum simulations of materials, J. Phys.: Condens. Matter **21**, 395502 (2009).
- [39] P. Giannozzi, O. Andreussi, T. Brumme, O. Bunau, M. B. Nardelli, M. Calandra, R. Car, C. Cavazzoni, D. Ceresoli, M. Cococcioni, *et al.*, Advanced capabilities for materials modelling with Quantum ESPRESSO, J. Phys.: Condens. Matter **29**, 465901 (2017).
- [40] A. Dal Corso, Pseudopotentials periodic table: From H to Pu, Comput. Mater. Sci. **95**, 337 (2014).
- [41] N. Marzari, A. A. Mostofi, J. R. Yates, I. Souza, and D. Vanderbilt, Maximally localized Wannier functions: Theory and applications, Rev. Mod. Phys. **84**, 1419 (2012).
- [42] G. Guo, Y. Yao, and Q. Niu, Ab initio calculation of the intrinsic spin Hall effect in semiconductors, Phys. Rev. Lett. **94**, 226601 (2005).
- [43] Y. Yao and Z. Fang, Sign changes of intrinsic spin hall effect in semiconductors and simple metals: First-principles calculations, Phys. Rev. Lett. **95**, 156601 (2005).
- [44] J. H. Ryoo, C.-H. Park, and I. Souza, Computation of intrinsic spin Hall conductivities from first principles using maximally localized Wannier functions, Phys. Rev. B **99**, 235113 (2019).
- [45] S. Ponce, E. R. Margine, C. Verdi, and F. Giustino, Epw: Electron–phonon coupling, transport and superconducting properties using maximally localized Wannier functions, Comput. Phys. Commun. **209**, 116 (2016).
- [46] G. Y. Guo, S. Murakami, T.-W. Chen, and N. Nagaosa, Intrinsic spin Hall effect in Platinum: First-principles calculations, Phys. Rev. Lett. **100**, 465901 (2008).

- [47] G. M. Stiehl, R. Li, V. Gupta, I. El Baggari, S. Jiang, H. Xie, L. F. Kourkoutis, K. F. Mak, J. Shan, R. A. Buhrman, *et al.*, Layer-dependent spin-orbit torques generated by the centrosymmetric transition metal dichalcogenide β - MoTe₂, Phys. Rev. B **100**, 184402 (2019).
- [48] G. Pizzi, D. Volja, B. Kozinsky, M. Fornari, and N. Marzari, Boltzmann: A code for the evaluation of thermoelectric and electronic transport properties with a maximally-localized Wannier functions basis, Comput. Phys. Commun. **185**, 422 (2014).